materials

MDPI

Article

Mechanistic Insights into CO_2 Adsorption of Li_4SiO_4 at High Temperature

Nan Ma [1,2,*], Silin Wei [1], Jinglin You [2], Fu Zhang [3] and Zhaohui Wu [1]

[1] Hunan Key Laboratory of Applied Environmental Photocatalysis, School of Materials and Environmental Engineering, Changsha University, Changsha 410022, China; w1625272361@163.com (S.W.); hubeiwzh1624@126.com (Z.W.)
[2] State Key Laboratory of Advanced Special Steel, Shanghai Key Laboratory of Advanced Ferrometallurgy, School of Materials Science and Engineering, Shanghai University, Shanghai 200444, China; jlyou@163.com
[3] State Key Laboratory of Applied Organic Chemistry, Key Laboratory of Nonferrous Metal Chemistry and Resources Utilization of Gansu Province, College of Chemistry and Chemical Engineering, Lanzhou University, Lanzhou 730000, China; fuzhang201026@163.com
* Correspondence: doria_mn@163.com

Abstract: The development of materials with high adsorption capacity for capturing CO_2 from industrial exhaust gases has proceeded rapidly in recent years. Li_4SiO_4 has attracted attention due to its low cost, high capture capacity, and good cycling stability for direct high-temperature CO_2 capture. Thus far, the CO_2 adsorption mechanism of Li_4SiO_4 is poorly understood, and detailed phase transformations during the CO_2 adsorption process are missing. Here, aided by in situ X-ray diffraction and in situ Raman spectroscopy, we find that Li_4SiO_4 reacts with CO_2 to form Li_2SiO_3 and Li_2CO_3 in CO_2 atmosphere at 973 K, with no detectable involvement of crystalline Li_2O during the adsorption process. Moreover, we observe a formation of stepped structures in the Li_4SiO_4 surface after CO_2 adsorption by scanning electron microscopy. To illustrate the formation of stepped structures, we propose a modified double-shell mechanism, suggesting a possible two-dimensional nucleation and growth of Li_2CO_3. This work provides a deeper understanding of the CO_2 adsorption mechanism and paves a way for further optimization of Li_4SiO_4-based adsorbents.

Keywords: CO_2 adsorbent; in situ X-ray diffraction; in situ Raman spectroscopy; adsorption mechanism

check for updates

Academic Editor: Eri Yoshida

Received: 20 December 2024
Revised: 6 January 2025
Accepted: 9 January 2025
Published: 12 January 2025

Citation: Ma, N.; Wei, S.; You, J.; Zhang, F.; Wu, Z. Mechanistic Insights into CO_2 Adsorption of Li_4SiO_4 at High Temperature. *Materials* **2025**, *18*, 319. https://doi.org/10.3390/ma18020319

Copyright: © 2025 by the authors. Licensee MDPI, Basel, Switzerland. This article is an open access article distributed under the terms and conditions of the Creative Commons Attribution (CC BY) license (https://creativecommons.org/licenses/by/4.0/).

1. Introduction

Carbon dioxide (CO_2), a primary greenhouse gas emitted from industrial activities and daily life, significantly impacts global climate and environmental systems [1]. Employing CO_2 adsorbents can effectively mitigate CO_2 emissions in industrial processes, and the captured CO_2 serve as a valuable carbon resource with diverse applications across various sectors of the national economy, including uses as chemical raw materials, refrigerants, oilfield stimulation agents, inert solvents, and pressure sources [2–4].

Extensive research has been reported on using activated carbon [5], organic amines [6], calcium-based materials [7], and lithium-based materials [8] as potential candidates for CO_2 adsorbents. Among them, lithium orthosilicate (Li_4SiO_4) stands out due to its low cost, high capture capacity, and good cycling stability for direct high-temperature CO_2 capture, making it an ideal adsorbent for separating CO_2 from flue gases [9–14]. Ever since the proposal of Li_4SiO_4 as a high-temperature CO_2 adsorbent by Kato et al. [15] in 2002, numerous studies have emerged mainly focusing on improving CO_2 adsorption

performance though condition control [16–18], impurity doping [19,20], and structural improvements [21–23].

To further enhance CO_2 adsorption performance, understanding the adsorption mechanism is crucial. Kato et al. [15,22] suggested that the adsorption process involves a reversible reaction between Li_2O in the Li_4SiO_4 crystal structure and CO_2. They pointed out that the diffusion of Li_2O to the Li_4SiO_4 surface is considered as the rate-limiting step at a higher CO_2 concentration, while the surface reaction becomes the rate-limiting step for lower CO_2 concentrations [24]. Zhang et al. [17,18] proposed a double-shell mechanism to explain the reaction of Li_4SiO_4 with CO_2. They declared that the products, Li_2SiO_3 and Li_2CO_3, cover the unreacted Li_4SiO_4, separating into two product layers, with the Li_2SiO_3 being the inner layer and the Li_2CO_3 the outer layer [17,18]. Subsequently, the unreacted Li_4SiO_4 generates O^{2-} and Li^+ ions, which diffuse outward through the Li_2SiO_3 shell and react with CO_2 that has diffused inward through the Li_2CO_3 shell [17,18]. Most recently, though creative inert-marker experiments, Deng et al. [25] reported that the dominant diffusion mode in the product layers only involves the outward diffusion of O^{2-} and Li^+ ions rather than the diffusion of Li_2O or CO_2, and the O^{2-} ion first diffuses outward to the surface and reacts with CO_2 to form CO_3^{2-}, while Li^+ ions diffuse outward and react with CO_3^{2-} to form Li_2CO_3. However, to further confirm the CO_2 adsorption mechanism of Li_4SiO_4, the in situ observations [26–28] of phase transformations during the CO_2 adsorption process still remain to be examined.

In this work, we carried out a comprehensive investigation of the CO_2 capture performances of Li_4SiO_4 adsorbent and the associated phase transformations during the CO_2 adsorption process. This was achieved through a combination of thermogravimetric (TG) analysis, in situ X-ray diffraction (XRD), in situ Raman spectroscopy analysis, and density functional theory (DFT) calculations. Additionally, scanning electron microscopy (SEM) was utilized to characterize the surface morphology of the Li_4SiO_4 adsorbent both before and after CO_2 adsorption. Finally, we proposed a modified double-shell model to elucidate the underlying mechanism of the CO_2 adsorption process.

2. Materials and Methods

2.1. Material Synthesis

Analytical reagent grade Li_2CO_3 and SiO_2, both sourced from Sinopharm Chemical Reagent Co., Ltd., Shanghai (China), were used in the present work. All the chemicals were dried at 473 K for 2 h to remove the surface moisture. Stoichiometric amounts of Li_2CO_3 and SiO_2 were initially mixed and ground in an agate mortar with an appropriate amount of ethanol for 1 h, then transferred into a corundum crucible. The mixture was synthesized at a temperature of 1123 K for a period of 6 h in an air atmosphere. The resultant products were subsequently ground for further analyses.

2.2. Material Characterization

The in situ X-ray powder diffraction (XRD) measurements were conducted using the Bruker D8 Advance X-ray diffractometer (Bruker AXS, Karlsruhe, Germany) (40 KV, 40 mA) with Cu/Kα1 radiation (λ = 0.15406 nm). In the heating process, the patterns were recorded in N_2 atmosphere in the 2θ range of 10° to 90° with a step size of 0.02° and a counting time of 0.1 s per step.

The in situ Raman spectroscopy measurements were carried by using a Horiba Jobin Y'von LabRAM HR Evolution Raman spectrometer (Horiba Jobin Y'von, Paris, France). The microscopic heating furnace was a Linkam TS1500 (Linkam, Tadworth, UK) with a temperature deviation within $\pm$1 K. The laser wavelength is 532 nm (Coherent, Santa Clara, CA, USA), and the integration time is 10 s 10 time.

The in situ XRD and in situ Raman spectroscopy have the same heating program. The heating rate is 10 K/min, with a N_2 flow rate of 45 cm^3/min. When the temperature rises to 973 K, the atmosphere changes from N_2 to CO_2, holding for 150 min. During the heat preservation period, the spectrum was measured every ten minutes.

The thermogravimetric (TG) analyses were performed by the Netzsch STA449F5 simultaneous thermal analyzer (Netzsch, Stuttgart, Germany). During the initial heating process, both the protective and purge gases were N_2, with a gas flow rate of 20 cm^3/min and a heating rate of 10 K/min. When the temperature reached 973 K, the purge gas was switched from N_2 to CO_2, and the flow rate for both the protective and purge gases was increased to 45 cm^3/min. The system was then maintained at this temperature for 150 min.

A Zeiss Sigma 300 scanning electron microscope (SEM) (Carl Zeiss AG, Oberkochen, Germany) was used to determine the morphology of Li_4SiO_4 particles before and after CO_2 adsorption. All samples were sputter-coated with Au before the measurements due to the poor electron conductivity of Li_4SiO_4.

2.3. Computational Details

Density functional theory (DFT) calculations were performed using the Cambridge Serial Total Energy Package (CASTEP) code (Materials Studio 8.0) [29,30]. The Raman wavenumber and intensity of various vibration modes of Li_4SiO_4, Li_2SiO_3, and Li_2CO_3 crystals were used by the functional set LDA (CA−PZ) version [31,32] with optimized norm-conserving pseudopotentials [33]. A plane wave energy cut-off of 600 eV was used for all computations. The *k*-point meshes were set as 3 × 3 × 3 for all structures. The convergence criterion for the electronic self-consistent field was set to 2×10^{-6} eV, and the maximum atomic force was determined to be 0.02 eV/Å. All the initial crystal structures were obtained from the Inorganic Crystal Structure Database (ICSD) [34].

3. Results and Discussion

3.1. Characterization of the Pristine Li_4SiO_4

Figure 1a shows the room-temperature XRD pattern of the pristine Li_4SiO_4 sample. The diffraction peaks of pristine Li_4SiO_4 corresponded well with the main reflections at 2θ = 22.2°, 22.6°, 33.8°, and 34.8° of the standard monoclinic phase of Li_4SiO_4, demonstrating the successful preparation of Li_4SiO_4. In addition, it is noteworthy that no XRD diffraction peaks for Li_2O are observed.

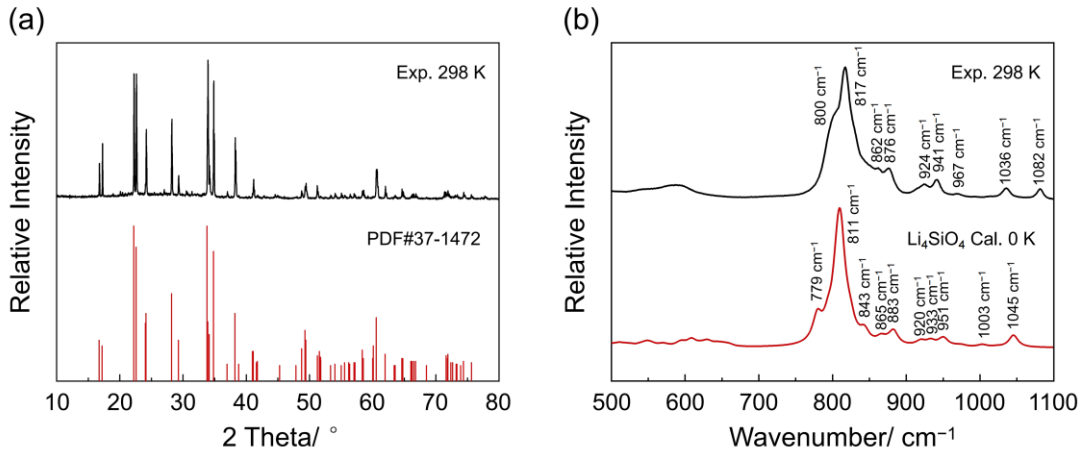


Figure 1. (**a**) XRD pattern of pristine Li_4SiO_4. (**b**) Calculated and measured Raman spectra of pristine Li_4SiO_4.

Li_4SiO_4 crystallizes in the monoclinic $P2_1/m$ space group. The unit cell of Li_4SiO_4 (ICSD No. 35169) contains fourteen formula units ($Li_8Si_2O_8$) with lattice a = 5.147 Å, b = 6.094 Å, c = 5.293 Å, α = 90°, β = 90.33°, γ = 90°, and V = 166.017 Å^3 [35]. Figure S1 (see the supplementary materials) shows the unit cell of Li_4SiO_4 which contains two SiO_4 tetrahedra which are isolated from one another. Based on the crystal structure of Li_4SiO_4, we obtained the theoretical Raman spectrum of Li_4SiO_4 by DFT calculations. As shown in Figure 1b, there are five main peaks observed at 779, 811, 883, 951, and 1045 cm^{-1} in the theoretical spectrum. Notably, the bands at 779, 811, 883, and 1045 cm^{-1} correspond to the symmetrical stretching vibrational modes of the Si–O bonds of isolated SiO_4 tetrahedra. In addition, the band located at 951 cm^{-1} belongs to the rocking vibration modes of the Si–O bonds. The major calculated vibrational modes of the Li_4SiO_4 crystal are listed in Table 1. In addition, the peak shapes of the measured Raman spectra of pristine Li_4SiO_4 are consistent with previous results [14]. Five peaks at 800, 817, 876, 967, and 1082 cm^{-1} are assigned to Li_4SiO_4, according to the theoretical Raman spectrum. In addition, according to previous reports, if Li_2O exists, its peak might appear around 534 cm^{-1} [36]. However, in the experimental Raman spectrum of pristine Li_4SiO_4, no peaks corresponding to Li_2O are observed. Notably, the overall peaks of the theoretical Raman spectrum are slightly lower than those of the experimental spectrum, which could be attributed to the DFT calculations being conducted at 0 K, without taking into account the influence of temperature.

Table 1. The assignment of major vibration modes of crystalline Li_4SiO_4.

Wavenumber		Vibration Modes	Type of Vibration
υ_{exp} (cm^{-1})	υ_{cal} (cm^{-1})		
800	779	A_g	υ_s(Si–O)
817	811	A_g	υ_s(Si–O)
862	865	B_g	υ_r(Si–O)
876	883	A_g	υ_s(Si–O)
924	920	A_g	υ_s(Si–O)
941	933	A_g	υ_s(Si–O)
967	951	B_g	υ_r(Si–O)
1036	1003	A_g	υ_s(Si–O)
1082	1045	A_g	υ_s(Si–O)

υ_s and υ_r represent the symmetric stretching vibrations and the rocking vibrations.

3.2. CO_2 Capture Performance

The influence of temperature on the CO_2 adsorption process was analyzed in the pure CO_2 atmosphere. Figure 2 shows the CO_2 adsorption performance on Li_4SiO_4 at different temperatures. The overall weight gain of Li_4SiO_4 increases with the temperature in the range from 773 to 973 K. Over a duration of 150 min, the weight gain of Li_4SiO_4 reaches 4.95, 8.49, 11.01, and 14.84% at 773, 823, 873, and 923 K, respectively, without reaching dynamic equilibrium. However, the weight gain of Li_4SiO_4 reaches 32.30% at 973 K, with dynamic equilibrium being reached, which aligns with the previous research result of 33.77% [17]. We believe that these differences can be attributed to the differences in particle size. Moreover, the weight gain of Li_4SiO_4 drops to zero at 1023 K, indicating that the adsorption reaction does not occur at this temperature. This observation aligns with the previously reported adsorption reaction temperature range of approximately 500 to 715 °C [13]. Consequently, the optimal temperature of Li_4SiO_4 for CO_2 adsorption is considered to be 973 K, with the peak adsorption capacity of 0.323 g CO_2/g Li_4SiO_4. This is slightly lower than the theoretical CO_2 adsorption capacity of 0.367 g CO_2/g Li_4SiO_4, as predicted by the reaction equation $Li_4SiO_4 + CO_2 \rightarrow Li_2SiO_3 + Li_2CO_3$.

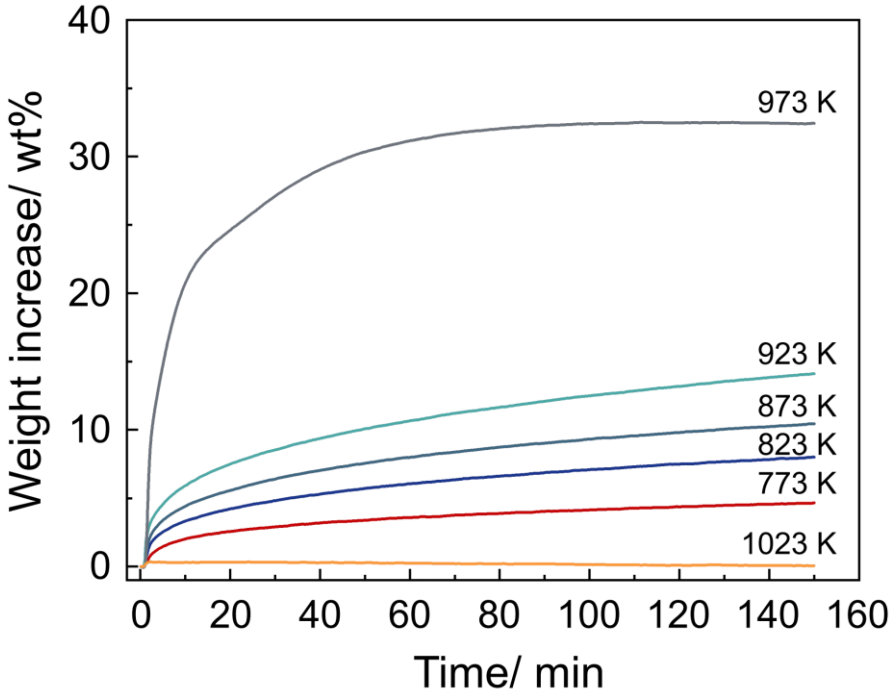


Figure 2. The CO_2 adsorption curves of Li_4SiO_4 over time under pure CO_2 atmosphere at different temperatures.

3.3. Phase Evolution via In Situ XRD and In Situ Raman Spectroscopy

To investigate the thermal stability of Li_4SiO_4, in situ XRD experiments were performed under inert N_2 gas. Figure 3a shows the in situ XRD patterns of Li_4SiO_4 heating from room temperature to 973 K in N_2 atmosphere. The XRD spectra show no significant changes during the heating process. The diffraction peaks correspond well with the standard monoclinic phase of Li_4SiO_4, while no diffraction peaks for crystalline Li_2SiO_3 or Li_2O are observed. These indicate that the Li_4SiO_4 maintains the same phase when the temperature was raised from room temperature to 973 K in N_2 atmosphere.

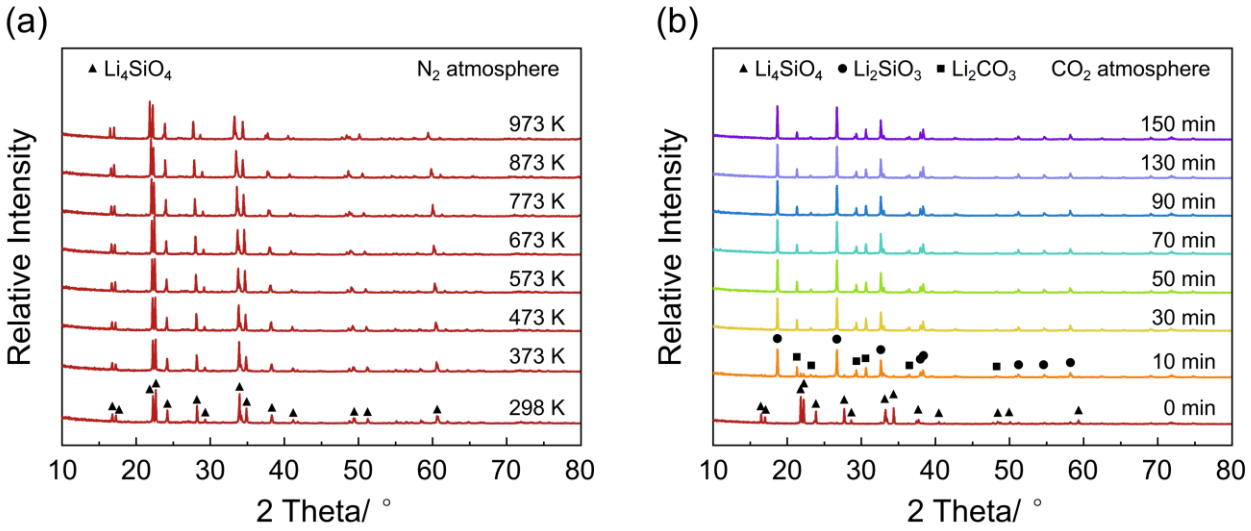


Figure 3. (**a**) In situ XRD patterns of Li_4SiO_4 heating from room temperature to 973 K in N_2 atmosphere. (**b**) In situ XRD patterns of Li_4SiO_4 during CO_2 adsorption process at 973 K in CO_2 atmosphere.

In order to obtain the phase transformation during the CO_2 adsorption process of Li_4SiO_4, in situ XRD was performed under CO_2 reaction conditions at 973 K. Figure 3b shows the in situ XRD patterns of Li_4SiO_4 during the CO_2 adsorption process at 973 K in CO_2 atmosphere. After the adsorption reaction at 973 K in CO_2 atmosphere for 10 min, two groups of new peaks appear. The first group of new peaks, corresponding to the new orthorhombic phase of Li_2SiO_3, is observed at 18.9°, 27.0°, and 33.1°, while the second group of new peaks appears at 21.3°, 30.6°, and 31.8°, assigned to the new monoclinic phase of Li_2CO_3. Subsequently, as the reaction time increases, the peaks assigned to Li_4SiO_4 quickly disappear, and the peaks of Li_2SiO_3 and Li_2CO_3 become dominant. Moreover, no crystalline peaks of Li_2O were observed in the in situ XRD spectra. There could be several possible reasons: (1) Li_2O does not form during the reaction process, (2) Li_2O, being a metastable phase, might have a very short lifespan and immediately react with CO_2 to form Li_2CO_3, and (3) Li_2O might exist in an amorphous state, which makes its detection challenging.

Li_2SiO_3 crystallizes in the orthorhombic $Ccm2_1$ space group. The unit cell of Li_2SiO_3 (ICSD No. 35169) contains four formula units ($Li_8Si_4O_{12}$) with lattice a = 5.398 Å, b = 9.397 Å, c = 4.661 Å, $\alpha = \beta = \gamma = 90°$, and V = 236.209 Å^3 [37]. As illustrated in Figure S2, the unit cell of Li_2SiO_3 contains four SiO_4 tetrahedra and eight Li ions. However, unlike in Li_4SiO_4, the SiO_4 tetrahedra in Li_2SiO_3 are not isolated; instead, they are connected to adjacent SiO_4 tetrahedra through the bridging vertex oxygen ions, forming a chain-like structure (Figure S2). Li_2CO_3 crystallizes in the monoclinic $C2/c$ space group. The unit cell of Li_2CO_3 (ICSD No. 16713) also contains four formula units ($Li_8C_4O_{12}$) with lattice a = 8.359 Å, b = 4.977 Å, c = 6.194 Å, $\alpha = 90°$, β= 114.72°, $\gamma = 90°$, and V = 233.778 Å^3 [38]. As shown in Figure S3, the unit cell of Li_2CO_3 contains four planar covalently bonded $[CO_3]^{2-}$ groups and eight Li ions. According to the crystal structure of Li_2SiO_3 and Li_2CO_3, we obtained the theoretical Raman spectra of Li_2SiO_3 and Li_2CO_3 by DFT calculations. As shown in Figure 4, seven main peaks are observed at 314, 351, 394, 497, 596, 969, and 1026 in the theoretical spectrum of Li_2SiO_3. The bands observed at 314, 394, 497, 596, and 969 cm^{-1} are attributed to the symmetrical stretching vibrational modes of the Si–O_{nb} (where O_{nb} represents the non-bridging oxygen) bonds, while the bands located at 351 and 1026 cm^{-1} are associated with the symmetrical stretching vibrational modes of the Si–O_b (where O_b represents the bridging oxygen) bonds. Figure 4 additionally presents shows the theoretical Raman spectrum of Li_2CO_3. The characteristic peak of the calculated Raman spectrum of Li_2CO_3 is located at 1088 cm^{-1}, corresponding to the symmetrical stretching vibrational modes of the C–O bonds in planar covalently bonded $[CO_3]^{2-}$. The major calculated vibrational modes of the Li_4SiO_4 and Li_2CO_3 are listed in Table 2.

To further confirm the in situ XRD analysis results, in situ Raman spectroscopy experiments were conducted under inert N_2 gas and CO_2 reaction conditions, respectively. Figure 5a shows the in situ Raman spectra of Li_4SiO_4 heating from room temperature to 973 K in N_2 atmosphere. The Raman spectra of Li_4SiO_4 exhibit clear evidence of band broadening, with no emergence of new peaks during the heating process. This indicates that there is no phase transformation in Li_4SiO_4 when the temperature was heated from room temperature to 973 K in a N_2 environment, which is consistent with the in situ XRD analysis results mentioned above. Figure 5b shows the in situ Raman spectra of Li_4SiO_4 during the CO_2 adsorption process at 973 K in CO_2 atmosphere. It can be observed that several new peaks at 221, 318, 347, 510, 601, 969, 1016, and 1080 cm^{-1} appear after the N_2 atmosphere is switched to CO_2 atmosphere for 10 min at 973 K. The seven peaks at 221, 318, 347, 510, 601, 969, and 1016 cm^{-1} are assigned to Li_2SiO_3, according to the calculated Raman spectrum of Li_2SiO_3. In addition, the band observed at 1080 cm^{-1} is attributed to Li_2CO_3. These results correspond well with the DFT calculations and previous experimental studies [39–41].

Subsequently, as the reaction time increases, the peaks of the Raman spectra of Li_4SiO_4 quickly disappear and the peaks of the Li_2SiO_3 and Li_2CO_3 phases become dominant, which is also consistent with the in situ XRD analysis results mentioned above. The results of the in situ XRD and in situ Raman spectroscopy indicate that Li_4SiO_4 reacted with CO_2 to form Li_2SiO_3 and Li_2CO_3 in CO_2 atmosphere at 973 K, with no detectable involvement of crystalline Li_2O during the adsorption process. These findings do not support the previous assumption made by Kato et al. [15,22] that the adsorption process involves a reversible reaction between Li_2O in the Li_4SiO_4 crystal structure and CO_2.

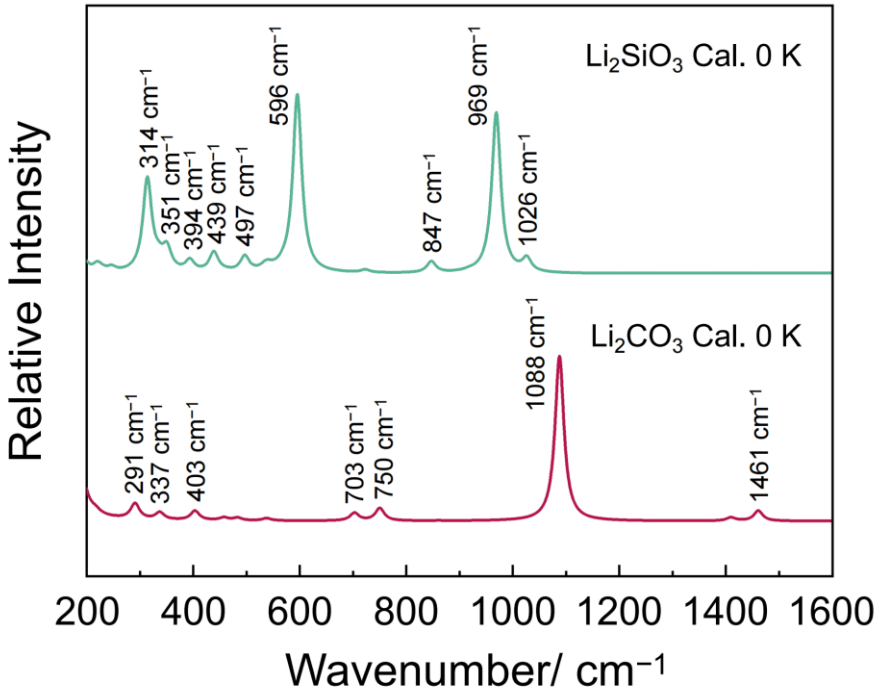


Figure 4. Calculated Raman spectra of Li_2SiO_3 and Li_2CO_3.

Table 2. The assignment of major vibration modes of crystalline Li_4SiO_4 in carbon dioxide atmosphere at 973 K.

Wavenumber		Vibration Modes	Type of Vibration
υ_{exp} (cm^{-1})	υ_{cal} (cm^{-1})		
318	351	A_2	υ_s (Si–O_b)
347	394	A_1	υ_s (Si–O_{nb})
396	439	A_1	υ_s (Si–O_{nb})
510	497	A_1	υ_s (Si–O_{nb})
601	596	A_1	υ_s (Si–O_{nb})
705	703	A_g	υ_s (C–O)
729	750	B_g	υ_r (C–O)
842	847	A_1	υ_s (Si–O_{nb})
969	969	A_1	υ_s (Si–O_{nb})
1016	1026	A_2	υ_s (Si–O_b)
1080	1088	A_g	υ_s (C–O)
1410	1461	A_g	υ_s (C–O)

υ_s and υ_r represent the symmetric stretching vibrations and the rocking vibrations.

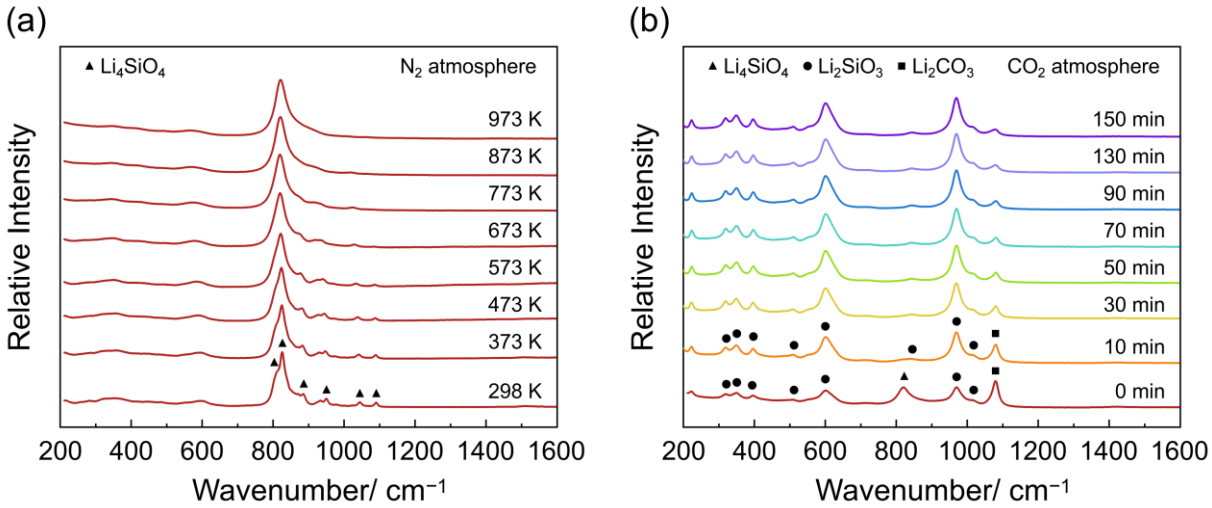


Figure 5. (**a**) In situ Raman spectra of Li_4SiO_4 heating from room temperature to 973 K in N_2 atmosphere. (**b**) In situ Raman spectra of Li_4SiO_4 during CO_2 adsorption process at 973 K in CO_2 atmosphere.

3.4. Morphology of Li_4SiO_4 Before and After CO_2 Adsorption

Figure 6 shows the SEM images of the pristine Li_4SiO_4 samples before and after CO_2 adsorption. Before CO_2 adsorption, the sample exhibits a relatively dense and smooth surface (Figure 6a). This morphology aligns with the SEM results presented in previous studies [17], suggesting that Li_4SiO_4 can be considered as a non-porous material. In addition, the smooth surfaces may correspond to some specific crystallographic plane of Li_4SiO_4. After CO_2 adsorption, distinct stepped structures are formed (Figure 6b), while the surface of the sample becomes looser and exhibits several minor cracks. The stepped structures were also observed by Zhang and colleagues in their research [18]. We assumed the formation of the stepped morphology may be due to the two-dimensional nucleation and growth [42] or the step-edge-guided nucleation and growth of the products [43,44].

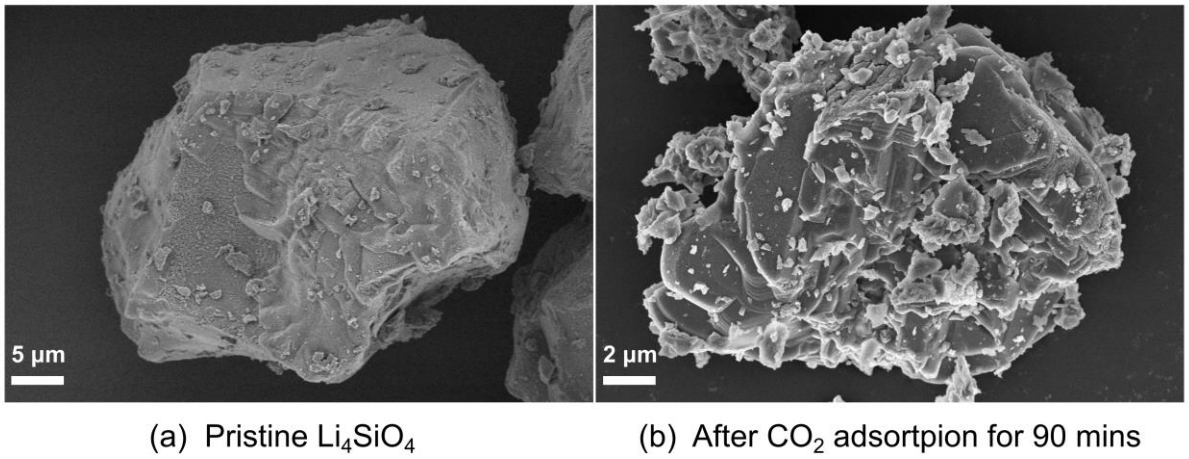


Figure 6. SEM images of Li_4SiO_4 before (**a**) and after (**b**) CO_2 adsorption for 90 min.

3.5. CO_2 Adsorption Mechanism of Li_4SiO_4

The CO_2 adsorption process on Li_4SiO_4 is generally considered to occur in two stages: initially, the adsorption stage, which is controlled by the fast surface chemical reactions, followed by the diffusion stage, governed by slower diffusion kinetics [45]. Based on the double-shell mode [17,18], we proposed a modified mode to illustrate the reaction mechanism. The whole absorption process involves the following procedures:

1. Adsorption stage: A CO_2 molecule will be adsorbed on the Li_4SiO_4 surface first (Figure 7a) due to a large adsorption energy [45,46]. The C atom in CO_2 forms a bond with a surface O^{2-} ion of Li_4SiO_4, and the two oxygen atoms of CO_2 are coordinated to the two surface Li^+ ions of Li_4SiO_4 [46]. Then, more adsorbed CO_2 molecules react with Li_4SiO_4 to form the Li_2SiO_3 and Li_2CO_3 nuclei, as shown in Figure 7b. Subsequently, Li_2SiO_3 gradually grows to cover the unreacted Li_4SiO_4, and simultaneously, Li_2CO_3 forms a layer outside the Li_2SiO_3. This leads to the formation of a double-shell structure: the outer shell consists of Li_2CO_3, the inner shell is composed of Li_2SiO_3, and the core remains as unreacted Li_4SiO_4 (Figure 7c).
2. Diffusion stage: According to previous literature reports, CO_2 molecules cannot diffuse through the Li_2SiO_3 and Li_2CO_3 shells [25]. However, Li^+ and O^{2-} ions, which are formed by the unreacted Li_4SiO_4 at the interface between Li_2SiO_3 and the remaining unreacted Li_4SiO_4, are capable of diffusing through these two shells [25,47,48]. As the reaction proceeds, the Li^+ and O^{2-} ions react with CO_2 molecules at the surface of the existing Li_2CO_3 layer, leading to the two-dimensional nucleation and growth of Li_2CO_3, as shown in Figure 7d. In a similar manner, new two-dimensional nuclei of Li_2CO_3 continue to form on the surface of the newly generated Li_2CO_3. This process results in different layers of Li_2CO_3, which form a stepped structure, and growth of Li_2CO_3 persists along the edges of these steps, as depicted in Figure 7e. Finally, the double shells become thicker until the reaction is fully completed (Figure 7f).

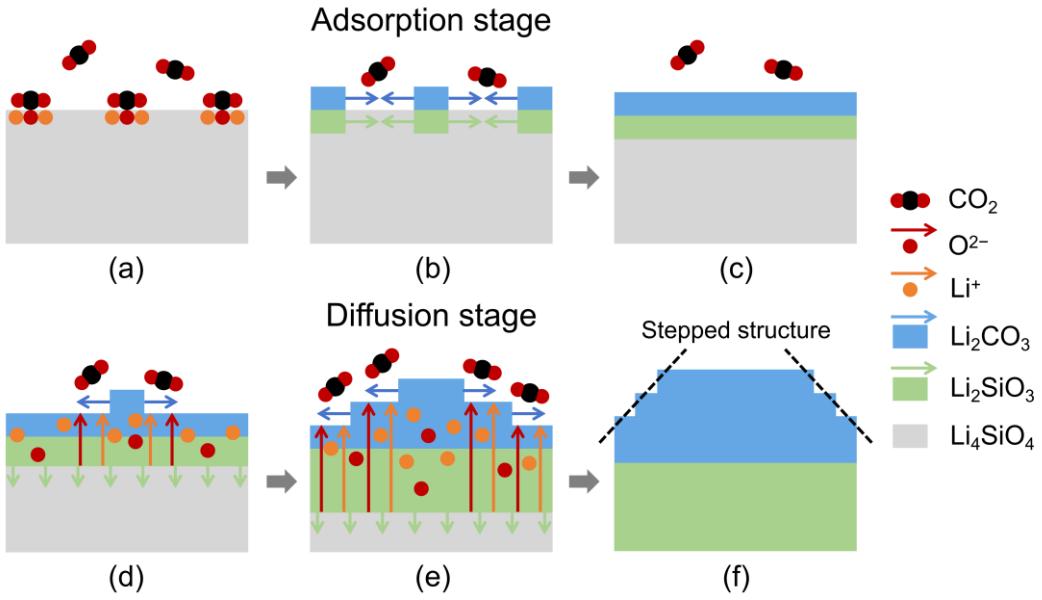


Figure 7. The illustration of reaction mechanism of Li_4SiO_4 during the CO_2 adsorption process. (**a**) Initial CO_2 adsorption on Li_4SiO_4. (**b**) Formation of Li_2SiO_3 and Li_2CO_3 nuclei. (**c**) Formation of double-shell structure. (**d**) Two-dimensional nucleation and growth of Li_2CO_3. (**e**) Formation of stepped structure as Li_2CO_3 layers continue to form. (**f**) Completion of the process as the double shells thicken.

4. Conclusions

In conclusion, the Li_4SiO_4 absorbent was successfully synthesized by solid-state reaction. The maximum CO_2 adsorption capacity of Li_4SiO_4 in CO_2 atmosphere at 973 K reaches 0.323 g CO_2/g Li_4SiO_4, which is slightly lower than the theoretical value of 0.367 g CO_2/g Li_4SiO_4. To elucidate the CO_2 adsorption mechanism of Li_4SiO_4, in situ XRD and in situ Raman spectroscopy were used to study the phase transformations during the CO_2 adsorption process. We observed that Li_4SiO_4 reacted with CO_2 to form Li_2SiO_3 and Li_2CO_3, with no detectable involvement of crystalline Li_2O during the adsorption process. SEM images

further characterized the morphological changes in the Li_4SiO_4 surface before and after CO_2 adsorption, with the formation of stepped structures. Finally, a modified double-shell mechanism was proposed to elucidate the underlying mechanism of the CO_2 adsorption process. The possible cause of the formation of stepped structures might be attributed to the two-dimensional nucleation and growth of Li_2CO_3; this hypothesis, however, requires further investigation.

Supplementary Materials: The following supporting information can be downloaded at: https://www.mdpi.com/article/10.3390/ma18020319/s1, Figure S1: Schematic representation of the Li_4SiO_4 crystal structure. Key: SiO_4, blue tetrahedra; lithium, green. Partially occupied Li sites are represented by partial shading. Unit cells are shown as dotted lines. Figure S2: Schematic representation of the Li_2SiO_3 crystal structure. Key: SiO_4, blue tetrahedra; lithium, green. Unit cells are shown as dotted lines. Figure S3: Schematic representation of the Li_2CO_3 crystal structure. Key: CO_3, brown triangle; lithium, green. Unit cell is shown as dotted lines.

Author Contributions: Conceptualization, N.M. and S.W.; methodology, J.Y.; software, J.Y.; validation, N.M., F.Z. and Z.W.; formal analysis, N.M.; investigation, N.M. and S.W.; resources, N.M. and J.Y.; data curation, S.W. and F.Z.; writing—original draft preparation, N.M.; writing—review and editing, N.M. and Z.W.; visualization, N.M. and S.W.; supervision, N.M.; project administration, N.M. and J.Y.; funding acquisition, N.M. and J.Y. All authors have read and agreed to the published version of the manuscript.

Funding: This work was financially supported by the National Natural Science Foundation of China (Grant No. 21773152), China Postdoctoral Science Foundation (Grant No. 2022M722039), Scientific Research Fund of Hunan Provincial Education (Grant No. 24B0788), Open Project of State Laboratory of Advanced Special Steel (Grant No. SKLASS 2023-02), and Talent Introduction Project of Changsha University (Grant No. SF1916).

Institutional Review Board Statement: Not applicable.

Informed Consent Statement: Not applicable.

Data Availability Statement: The original contributions presented in this study are included in the article/Supplementary Material. Further inquiries can be directed to the corresponding author.

Conflicts of Interest: There are no conflicts to declare.

References

1. Shakun, J.D.; Clark, P.U.; He, F.; Marcott, S.A.; Mix, A.C.; Liu, Z.Y.; Otto-Bliesner, B.; Schmittner, A.; Bard, E. Global warming preceded by increasing carbon dioxide concentrations during the last deglaciation. *Nature* **2012**, *484*, 49–54. [CrossRef] [PubMed]
2. Nagireddi, S.; Agarwal, J.R.; Vedapuri, D. Carbon dioxide capture, utilization, and sequestration: Current status, challenges, and future prospects for global decarbonization. *ACS Eng. Au* **2023**, *4*, 22–48. [CrossRef]
3. Hu, Y.C.; Liu, W.Q.; Yang, Y.D.; Qu, M.Y.; Li, H.L. CO_2 capture by Li_4SiO_4 sorbents and their applications: Current developments and new trends. *Chem. Eng. J.* **2019**, *359*, 604–625. [CrossRef]
4. Zhang, Z.E.; Pan, S.Y.; Li, H.; Cai, J.C.; Olabi, A.G.; Anthony, E.J.; Manovic, V. Recent advances in carbon dioxide utilization. *Renew. Sustain. Energy Rev.* **2020**, *125*, 109799. [CrossRef]
5. Zhao, Y.F.; Liu, X.; Han, Y. Microporous carbonaceous adsorbents for CO_2 separation via selective adsorption. *RSC Adv.* **2015**, *5*, 30310–30330. [CrossRef]
6. Sayari, A.; Belmabkhout, Y. Stabilization of amine-containing CO_2 adsorbents: Dramatic effect of water vapor. *J. Am. Chem. Soc.* **2010**, *132*, 6312–6314. [CrossRef]
7. Sun, H.M.; Parlett CM, A.; Isaacs, M.A.; Liu, X.T.; Adwek, G.; Wang, J.Q.; Shen, B.X.; Huang, J.; Wu, C.F. Development of Ca/KIT-6 adsorbents for high temperature CO_2 capture. *Fuel* **2019**, *235*, 1070–1076. [CrossRef]
8. Xiao, Q.; Liu, Y.F.; Zhong, Y.J.; Zhu, W.D. A citrate sol-gel method to synthesize Li_2ZrO_3 nanocrystals with improved CO_2 capture properties. *J. Mater. Chem.* **2011**, *21*, 3838–3842. [CrossRef]
9. Tong, Y.C.; Qin, C.L.; Zhu, L.Y.; Chen, S.Z.; Lv, Z.Z.; Ran, J.Y. From spent Lithium-ion batteries to low-cost Li_4SiO_4 sorbent for CO_2 capture. *Environ. Sci. Technol.* **2022**, *56*, 5734–5742. [CrossRef]

10. Wang, K.; Zhao, P.F.; Guo, X.; Li, Y.M.; Han, D.T.; Chao, Y. Enhancement of reactivity in Li_4SiO_4-based sorbents from the nano-sized rice husk ash for high-temperature CO_2 capture. *Energy Convers. Manag.* **2014**, *81*, 447–454. [CrossRef]
11. Yang, Y.D.; Cao, J.X.; Hu, Y.C.; Sun, J.; Yao, S.; Li, Q.W.; Li, Z.X.; Zhou, S.M.; Liu, W.Q. Eutectic doped Li_4SiO_4 adsorbents using the optimal dopants for highly efficient CO_2 removal. *J. Mater. Chem. A* **2021**, *9*, 14309–14318. [CrossRef]
12. Belgamwar, R.; Maity, A.; Das, T.; Chakraborty, S.; Vinod, C.P.; Polshettiwar, V. Lithium silicate nanosheets with excellent capture capacity and kinetics with unprecedented stability for high-temperature CO_2 capture. *Chem. Sci.* **2021**, *12*, 4825–4835. [CrossRef] [PubMed]
13. Tong, Y.C.; Chen, S.Z.; Huang, X.; He, Y.; Chen, J.; Qin, C.L. CO_2 capture by Li_4SiO_4 sorbents: From fundamentals to applications. *Sep. Purif. Technol.* **2022**, *301*, 121977. [CrossRef]
14. Tan, Y.Y.; Zhang, X.Y.; Wei, W.; Hu, W.; Xing, H.Z.; Wang, S.T.; Liu, W.Q. Synthesis of high-performance Li_4SiO_4 sorbent for CO_2 capture using Li_2CO_3 extracted from spent lithium batteries. *Sep. Purif. Technol.* **2025**, *353*, 128605. [CrossRef]
15. Kato, M.; Yoshikawa, S.; Nakagawa, K. Carbon dioxide absorption by lithium orthosilicate in a wide range of temperature and carbon dioxide concentrations. *J. Mater. Sci. Lett.* **2002**, *21*, 485–487. [CrossRef]
16. OrtiAL, Z.; Bretado MA, E.; Velderrain, V.G.; Zaragoza, M.M.; Gutiérrez, J.S.; Gutiérrez, D.L.; Collins-Martínez, V. Experimental and modeling kinetic study of the CO_2 absorption by Li_4SiO_4. *Int. J. Hydrogen Energy* **2014**, *39*, 16656–16666.
17. Zhang, Q.; Han, D.Y.; Liu, Y.; Ye, Q.; Zhu, Z.B. Analysis of CO_2 sorption/desorption kinetic behaviors and reaction mechanisms on Li_4SiO_4. *AIChE J.* **2013**, *59*, 901–911.
18. Zhang, Q.; Peng, D.; Zhang, S.; Ye, Q.; Wu, Y.Q.; Ni, Y.H. Absorption behaviors and kinetic models analysis of Li_4SiO_4 under various CO_2 partial pressures. *AIChE J.* **2017**, *63*, 2153–2164. [CrossRef]
19. Zhao, D.L.; Geng, L.L.; Jia, Y.F.; Wei, J.W.; Zhou, X.B.; Liao, L. Adsorption of high-temperature CO_2 by Ca^{2+}/Na^{+}-doped lithium orthosilicate: Characterization, kinetics, and recycle. *Environ. Sci. Pollut. Res.* **2024**, *31*, 21267–21278. [CrossRef]
20. Zhao, P.F.; Wang, K.; Hong, J.; Anthony, E.J. High temperature capture of CO_2 on Li_4SiO_4 sorbents via a simple dry ball-milling coupled with K_2CO_3 physical addition. *Carbon Capture Sci. Technol.* **2024**, *13*, 100255. [CrossRef]
21. Rodríguez-Mosqueda, R.; Pfeiffer, H. Thermokinetic analysis of the CO_2 chemisorption on Li_4SiO_4 by using different gas flow rates and particle sizes. *J. Phys. Chem. A* **2010**, *114*, 4535–4541. [CrossRef] [PubMed]
22. Kato, M.; Nakagawa, K.; Essaki, K.; Maezawa, Y.; Takeda, S.; Kogo, R.; Hagiwara, Y. Novel CO_2 absorbents using lithium-containing oxide. *Int. J. Appl. Ceram. Technol.* **2005**, *2*, 467–475. [CrossRef]
23. Wu, X.W.; Wen, Z.Y.; Xu, X.G.; Wang, X.Y.; Lin, J. Synthesis and characterization of Li_4SiO_4 nano-powders by a water-based sol-gel process. *J. Nucl. Mater.* **2009**, *392*, 471–475. [CrossRef]
24. Essaki, K.; Kato, M.; Uemoto, H. Influence of temperature and CO_2 concentration on the CO_2 absorption properties of lithium silicate pellets. *J. Mater. Sci.* **2005**, *40*, 5017–5019. [CrossRef]
25. Deng, T.; Chen, S.Z.; Lv, Z.Z.; Zheng, Y.J.; Xu, S.J.; Qin, C.L. Ionic diffusion in CO_2 adsorption by Li_4SiO_4: Inert-marker experiment and DFT calculations. *Phys. Rev. Lett.* **2024**, *133*, 198001. [CrossRef]
26. Grasso, M.L.; Blanco, M.V.; Cova, F.; González, J.A.; Larochette, P.A.; Gennari, F.C. Evaluation of the formation and carbon dioxide capture by Li_4SiO_4 using in situ synchrotron powder X-ray diffraction studies. *Phys. Chem. Chem. Phys.* **2018**, *20*, 26570–26579. [CrossRef]
27. Hoyos, L.A.S.; Faroldi, B.M.; Cornaglia, L.M. K-doping effect in the kinetics of CO_2 capture at high temperature over lithium silicates obtained from rice husks: In situ/*operando* techniques. *Ceram. Int.* **2021**, *47*, 1558–1570. [CrossRef]
28. Wang, Z.R.; Liu, W.H.; Tang, Z.F.; Xu, Q. In situ Raman and XRD study of CO_2 sorption and desorption in air by a Na_4SiO_4-Na_2CO_3 hybrid sorbent. *Phys. Chem. Chem. Phys.* **2020**, *22*, 27263–27271. [CrossRef]
29. Segall, M.D.; Lindan PJ, D.; Probert, M.J.; Pickard, C.J.; Hasnip, P.J.; Clark, S.J.; Payne, M.C. First-principles simulation: Ideas, illustratiaons and the CASTEP code. *J. Phys.* **2002**, *14*, 2717–2744. [CrossRef]
30. Clark, S.J.; Segall, M.D.; Pickard, C.J.; Hasnip, P.J.; Probert MI, J.; Refson, K.; Payne, M.C. First principles methods using CASTEP. *Z. Krist.-Cryst. Mater.* **2005**, *220*, 567–570. [CrossRef]
31. Ceperley, D.M.; Alder, B.J. Ground state of the electron gas by a stochastic method. *Phys. Rev. Lett.* **1980**, *45*, 566–569. [CrossRef]
32. Perdew, J.P.; Zunger, A. Self-interaction correction to density-functional approximations for many-electron systems. *Phys. Rev. B* **1981**, *23*, 5048–5079. [CrossRef]
33. Hamann, D.R.; Schlüter, M.; Chiang, C. Norm-conserving pseudopotentials. *Phys. Rev. Lett.* **1979**, *43*, 1494–1497. [CrossRef]
34. Zagorac, D.; Müller, H.; Ruehl, S.; Zagorac, J.; Rehme, S. Recent developments in the inorganic crystal structure database: Theoretical crystal structure data and related features. *J. Appl. Crystallogr.* **2019**, *52*, 918–925. [CrossRef]
35. Völlenkle, H.; Wittmann, A.; Nowotny, H. Die Kristallstruktur von Li_4SiO_4. *Monatshefte Chem.* **1968**, *99*, 1360–1371. [CrossRef]
36. Hy, S.; Felix, F.; Rick, J.; Su, W.N.; Hwang, B.J. Direct in situ observation of Li_2O evolution on Li-rich high-capacity cathode material, $Li[Ni_xLi_{(1-2x)/3}Mn_{(2-x)/3}]O_2$ $(0 \leq x \leq 0.5)$. *J. Am. Chem. Soc.* **2014**, *136*, 999–1007. [CrossRef]
37. Hesse, K.F. Refinement of the crystal structure of lithium polysilicate. *Acta Crystallogr.* **1977**, *33*, 901–902. [CrossRef]
38. Zemann, J. Die Kristallstruktur von Li_2CO_3. *Acta Crystallogr.* **1957**, *10*, 664–666. [CrossRef]

39. Terry, R.J.; McMillen, C.D.; Chen, X.F.; Wen, Y.M.; Zhu, L.; Chumanov, G.; Kolis, J.W. Hydrothermal single crystal growth and second harmonic generation of Li_2SiO_3, Li_2GeO_3 and $Li_2Si_2O_5$. *J. Cryst. Growth* **2018**, *493*, 58–64. [CrossRef]
40. Heber, M.; Hess, C. Monitoring electrode/electrolyte interfaces of Li-ion batteries under working conditions: A surface-enhanced Raman spectroscopic study on $LiCoO_2$ composite cathodes. *Surf. Interface Anal.* **2022**, *54*, 847–854. [CrossRef]
41. Peltzer, D.; Salazar Hoyos, L.A.; Faroldi, B.; Múnera, J.; Cornaglia, L. Comparative study of lithium-based CO_2 sorbents at high temperature: Experimental and modeling kinetic analysis of the carbonation reaction. *J. Environ. Chem. Eng.* **2020**, *8*, 104173. [CrossRef]
42. Yan, N.N.; Fu, Q.G.; Zhang, J.P.; Shen, Q.L. Two-dimensional nucleation growth of stepped ZrC skeleton with controllable morphology. *Ceram. Int.* **2021**, *47*, 19090–19097. [CrossRef]
43. Zhao, K.; Lin, H.C.; Huang, W.T.; Hu, X.P.; Chen, X.; Xue, Q.K.; Ji, S.H. Molecular beam epitaxy growth of tetragonal FeS films on $SrTiO_3$(001) substrates. *Chin. Phys. Lett.* **2017**, *34*, 087401. [CrossRef]
44. Hao, J.G.; Zhang, Y.F.; Zhang, Y.J.; Xu, K.; Han, G.Q.; Ye, J.D. Step-edge-guided nucleation and growth mode transition of α-Ga_2O_3 heteroepitaxy on vicinal sapphire. *Chin. Phys. B* **2024**, *33*, 086104. [CrossRef]
45. Luo, G.Q.; Chen, J.Y.; Wang, J.X.; Zhu, B.Z.; Xu, M.G.; Yang, Y.; Sun, Y.L. Enhancement of CO_2 adsorption performance and widening of adsorption temperature window by co-doping different valence state metals on the Li_4SiO_4 (010) surface. *Ceram. Int.* **2024**, *50*, 9293–9306. [CrossRef]
46. Yu, W.J.; Xu, Q.; Li, S.G.; Xiong, X.L.; Cheng, H.W.; Zou, X.L.; Lu, X.G. Revealing the different performance of Li_4SiO_4 and Ca_2SiO_4 for CO_2 adsorption by density functional theory. *RSC Adv.* **2022**, *12*, 11190–11201. [CrossRef]
47. Shi, S.Q.; Lu, P.; Liu, Z.Y.; Qi, Y.; Hector, L.G., Jr.; Li, H.; Harris, S.J. Direct calculation of Li-ion transport in the solid electrolyte interphase. *J. Am. Chem. Soc.* **2012**, *134*, 15476–15487. [CrossRef]
48. Shi, S.Q.; Qi, Y.; Li, H.; Hector, L.G., Jr. Defect thermodynamics and diffusion mechanisms in Li_2CO_3 and implications for the solid electrolyte interphase in Li-ion batteries. *J. Phys. Chem. C* **2013**, *117*, 8579–8593. [CrossRef]

Disclaimer/Publisher's Note: The statements, opinions and data contained in all publications are solely those of the individual author(s) and contributor(s) and not of MDPI and/or the editor(s). MDPI and/or the editor(s) disclaim responsibility for any injury to people or property resulting from any ideas, methods, instructions or products referred to in the content.